

Controlled edge dependent stacking of WS₂-WS₂ Homo- and WS₂-WSe₂ Hetero-structures: A Computational Study

Kamalika Ghatak¹, Kyung Nam Kang², Eui-Hyeok Yang^{2,*}, Dibakar Datta^{1,*}

¹ Department of Mechanical and Industrial Engineering, New Jersey Institute of Technology, Newark, NJ 07103, USA

² Department of Mechanical Engineering, Stevens Institute of Technology, Hoboken, NJ 07030, USA

* Corresponding author (Email: eyang@stevens.edu, dibakar.datta@njit.edu)

Abstract

Transition Metal Dichalcogenides (TMDs) are one of the most studied two-dimensional materials in the last 5-10 years due to their extremely interesting layer dependent properties. Despite the presence of vast research work on TMDs, the complex relation between the electro-chemical and physical properties make them the subject of further research. Our main objective is to provide a better insight into the electronic structure of TMDs. This will help us better understand the stability of the bilayer post growth homo/hetero products based on the various edge-termination, and different stacking of the two layers. In this regard, two Tungsten (W) based non-periodic chalcogenide flakes (sulfides and selenides) were considered. An in-depth analysis of their different edge termination and stacking arrangement was performed via Density Functional Theory method using VASP software. Our finding indicates the preference of chalcogenide (*c*-) terminated structures over the metal (*m*-) terminated structures for both homo and heterobilayers, and thus strongly suggests the nonexistence of the *m*-terminated TMDs bilayer products.

1. Introduction:

The discovery of graphene has motivated researchers to find or synthesize similar novel two-dimensional (2D) structures for various practical applications. The non-bandgap nature associated with graphene hinders the implementation of 2D geometry in certain areas such as transistors, sensors, etc.¹ In this regard, various other 2D materials, including graphene, oxide, and chalcogen family, were explored and investigated after the discovery of graphene in 2004.² Among the new

generation 2D materials, Transition Metal Dichalcogenides (TMDs) are one of the most versatile materials owing to their wide variety of physicochemical, electrical, and mechanical properties that lie in between the semiconductor and metal.³⁻⁵ Moreover, the graphite-like features of the bulk-TMD crystals and possible graphene-like exfoliation of monolayer-TMDs, as well as the semi-honeycomb features, make them an attractive candidate. TMDs have the general formula MX_2 ($M = Mo$ and W ; $X = S, Se,$ and Te). The crystal structure of TMDs is three atoms thin, where one metal atom is sandwiched in between two chalcogen atoms ($X-M-X$) via strong covalent bonds (see Fig. 1b). These monolayer 2D TMDs are attached through weak van der Waals forces in the multilayered 3D crystal structures. Among various 2D TMDs, Molybdenum/Tungsten Sulfide/Selenides ($Mo/W S_2/Se_2$)⁶ are known to be stable at ambient conditions and thus are known to be useful for energy-storage, sensing, electronic and photonic devices applications.

Among the monolayer (ML) TMDs, the direct band gap of MoS_2 , WS_2 , and WSe_2 fall in the visible to the near-IR range and are therefore well explored for their significant electronic, optical and photocatalytic properties.^{3,7-11} ML MoS_2 is well studied¹²⁻¹⁸ for its transistor applications, excellent carrier mobility, as well as its potential applications in spintronics, valleytronics, bio, and gas sensing applications. On the other hand, WS_2 possesses similar crystal structure as of MoS_2 and, shows higher quantum efficiency, wider valence band maximum splitting and, lower effective mass of the carrier due to the presence of heavier W atom as compared to the Mo atom.¹⁹⁻²³ However, the synthesis of these ML 2D materials is the first step towards its practical application. The initial step begins with the exfoliation of ML WS_2 from the bulk crystal structures. Liquid exfoliation technique by Coleman et.al²⁴ and the mechanical exfoliation method by Zhang et.al²⁵ are the two most significant contributions towards the ML WS_2 synthesis. Among various chemical techniques, lithium intercalation in WS_2 powder, followed by the easy chemical exfoliation of the MLs, is also noteworthy.^{26,27}

Apart from the exfoliation methods, various other growth techniques such as Physical Vapor Deposition (PVD)²⁸⁻³⁰ and Chemical Vapor Deposition (CVD)^{31,32} techniques were adopted. Various CVD techniques using different substrates such as, on Si/SiO₂, Ti/TiO₂, Graphite, Graphene oxides, Sapphire, Au foil, *h*-BN etc. were also reported.³³⁻³⁹ Among several existing growth techniques, epitaxial CVD growth mechanism is the most preferred one due to its several technological advantages⁴⁰⁻⁴² such as reduction of defect density, consistency in the overall

growth, growth products with sharper interfaces, the perseverance of in-plane electrical conductivity via the introduction of mirror twin grain boundaries, and simultaneous reduction of tilt grain boundaries.⁴³⁻⁴⁵ However, these experimental growth techniques require further control over the layer thickness, edge sharpness, size, and the quality of the as-grown crystals in order to achieve specific applicability.³³ Along with the ML TMDs, synthesis of van der Waals 2D homo and heterostructures are also becoming an attractive field of research due to their layer dependent vast tunable properties.^{6,46,47} Therefore, it is essential to study the stable layered growth products and perform a thorough computational analysis in order to better understand the electronic and associated properties. In this respect, Density Functional Theory (DFT) study can provide deep insights of the edge and stacking dependency of the stable post growth products.

In this work, we have performed DFT calculations to get an in-depth understanding of the structural and electronic properties of homo/hetero bilayers of triangular WS₂, and WSe₂ flakes. We investigated the nature and strength of the interlayer interactions, by testing various combinations of AA and AB stacking. The most stable and unstable combinations were sorted based on their stacking energy and structural changes along with their electronic distribution. This comparative study also represents the important differences based on homo (WS₂-WS₂) and hetero bilayers (WS₂-WSe₂). This study aims to provide a crucial insight based on the existence of a specific combination of growth products towards the growth dynamics. Most of the existing studies on TMD heterostructures are based on periodic structures.⁴⁸⁻⁵¹ This work considers non-periodic structures, which are most commonly observed in experiments.⁵²⁻⁵⁴ Our results provide insight into the stability of the post-growth TMD homobilayers and heterobilayers.

2. Computational Methodology and Models

2.1 Methodology

All the electronic structure calculations were performed using the DFT method as implemented in the Vienna Ab initio Simulation Package (VASP).⁵⁵ Projector augmented wave (PAW) pseudopotential is taken for the inert core electrons, and valence electrons are represented by plane-wave basis set.^{56,57} The generalized gradient approximation (GGA), with the Perdew–

Becke–Ernzerhoff (PBE) exchange–correlation functionals, is taken into account.⁵⁸ In order to accurately estimate weak van der Waals interaction, a vdW-correction approach is used. The vdW-density functional (vdW-DF) combines nonlocal correlations directly within a DFT functional. All DFT based calculations in this study have been performed using the optPBE functional within the vdW-DFT family, implemented in the VASP package by Klimes and co-workers.⁵⁹⁻⁶¹ The plane wave basis was set up with a kinetic energy cutoff of 400 eV. Due to the non-periodic nature of the structure, the Brillouin zone is sampled using the gamma- k -point grid for each mono and bilayers. The box size was kept big enough in order to prevent the periodic image overlap. The distance between two periodic images was maintained to be more than 8 Å on each direction (details are present in the Section S1 of [supporting information \(SI\)](#)). The initial distances (W-W interlayer) between the two layers were kept in between the ~6.25–6.30 Å following the previous studies.^{62,63} The convergence criterion for the electronic relaxation was kept 10⁻⁵ eV/cell, and the total energy was calculated with the linear tetrahedron method with Blochl corrections. All the internal coordinates were relaxed using conjugate gradient methods until the Hellmann–Feynman forces are less than 0.02 eV/Å. In this study, all the atoms present in the systems were fully relaxed, and no atomic positions were fixed during the optimization method.

The free energy for stacking (stacking energy) was calculated using the following formula

$$\Delta G_f = G_{BL} - (G_{ML} + G_{ML'}) \quad (1)$$

Where, ΔG_f signifies the stacking energy of the bilayer TMD, and G_{BL} , G_{ML} or $G_{ML'}$ represent the total free energies of the bilayers and different monolayers. In case of homo-bilayers, ML and ML' represent the same mono-layers, but they represent different monolayers for the hetero-bilayers.

2.2 Models

Our study considers only zigzag edged TMD structures due to their well-known energetic and as well as various electronic preferences over the armchair ones.⁶⁴⁻⁷² In this regard, triangular MX₂ flakes are known to be zigzag edged from each side (see [Fig. 1c](#)), and they can either be transition metal terminated (m -) or chalcogen terminated (c -). More importantly, triangular flakes are one of the well-known geometries formed by the MLs.⁷³⁻⁷⁵ [Fig. 1a](#) represents the top view of the

hexagonal honeycomb geometry of an MX_2 flake with both armchair and zigzag edges. Top and bottom side of the figure represents the armchair edges, while, the left and right sides are the representative of the differently terminated zigzag edges. To understand the influence of the different edge termination towards the bilayer formation, one has to begin the analysis by considering either fully metal or chalcogen terminated MX_2 monolayer. In this study, we have investigated the stacking of triangular ML flakes and have considered both the homo and the hetero-bilayers cases. In the case of homo-bilayers, we have considered WS_2 - WS_2 . For WS_2 - WSe_2 hetero-bilayer, we have changed the chalcogen atoms (X) of one of the layers to *Se* from *S*. Apart from the edge termination, we have also considered the possible contribution of different stacking of this monolayer MX_2 flakes towards the formation of the bilayers. In order to do so, we have only focused on the two most important stacking possibilities vis a vis. AA and AB (see Fig. 2). Our investigation is focused on the zigzag edged WS_2 and WSe_2 monolayers (ML) with two different edge terminations - a) *m*-terminated (Fig. 1c1) and b) chalcogen (*c*) terminated (Fig. 1c2). Each of these monolayers (MLs) gets stacked together, forming bilayers (BLs) via two different stacking orientations named AA stacked (*m-m* and *c-c*), and AB stacked (*m-m* and *c-c*) as shown in Fig. 2. Here Fig. 2 is a general representation of all the homo/hetero layered (WS_2 - WS_2 (homo) and WS_2 - WSe_2 (hetero)) structures. AA is when the M and M (similarly X and X) sit on top of each other (Fig. 2a). On the other hand, AB represents the situation when M and X (similarly X and M) sit on top of each other (see Fig. 2b). It is important to mention here that due to the high computational cost and non-periodic nature of the models, small triangular flakes were considered to gain insight about the stacking phenomenon. Furthermore, the stacking of the triangular ML flakes was considered in order to fully understand the influence of edge termination of both layers and experimental reports on the stacking of triangular MLs were also present in the literature.^{76,77} Since the main purpose is to understand the edge effect, we haven't considered the edge termination/passivation.

3. Results and Discussion

3.1 Differently Stacked Homo/Hetero BLs Formation of WX_2 :

After performing a rigorous scaling process (details are given in the section S1 of the *SI*), we have optimized the following formula for the *c*- and *m*- terminated MLs: a) $W_{10}S_{30}$ (*c*-), b) $W_{10}S_{15}Se_{15}$ (*c*-), c) $W_{15}S_{20}$ (*m*-) and, d) $W_{15}S_{10}Se_{10}$ (*m*-). In this manner, we have the following formula for the BLs: $W_{20}S_{60}$ (homo-BL-*c*-AA and homo-BL-*c*-AB), $W_{20}S_{30}Se_{30}$ (hetero-BL-*c*-AA and hetero-BL-*c*-AB), $W_{30}S_{40}$ (homo-BL-*m*-AA and homo-BL-*m*-AB) and, $W_{30}S_{20}Se_{20}$ (hetero-BL-*m*-AA and hetero-BL-*m*-AB). We have relaxed the systems mentioned above to find stable orientations. [Fig. 3](#) represents the optimized structures for all the BLs, and [Fig. S1](#) of the *SI* represents the optimized structures of the above mentioned MLs. It is visually significant from [Fig. 3](#) that for both the AA and AB stacked homo/hetero BLs, *c*-terminated structures are less distorted as compared to their *m*-terminated counterparts. However, it is quite evident from [Fig. 3g](#) and [3h](#) that both the *m*-terminated AA/AB stacked heterobilayers are almost distorted from their original trigonal geometry.

To predict the stability of the afore-mentioned BL geometries, we have calculated the stacking energies (ΔG_f). Moreover, a proper structural analysis was also conducted before studying their electronic properties. [Table 1](#) and [2](#) depicts all the stacking energies values for the homo and hetero BLs respectively. High negative stacking energies of all the *c*-terminated BLs are also indicative of their extreme stability. On the other hand, low negative stacking energies of the *m*-terminated homo/hetero BLs strongly suggests the lower probability of their formation during the growth process. Most importantly, a moderately high positive stacking energy ([Table 2](#)) of the *m*-terminated AA stacked WS_2 - WSe_2 BL implies the non-existence of the same during the growth process. We also found that the *c*-terminated heterobilayers are more stable from their homo counterparts since they have higher negative stacking energies.

Structural analyses of these BLs and a comparative study with MLs is the first step to address the differences in the ΔG_f values. [Table 3](#) (*c*-terminated) and [4](#) (*m*-terminated) represents the average bond distances of all the BL and ML geometries. We have first considered the average interlayer W-W distances to get an insight of the same towards the stacking energy. In the case of *c*-terminated AA stacked BLs, both the homo and hetero W-W interlayer distances fall under the same range (~ 6.25 - 6.28 Å), which is comparable to the previously reported studies^{62,63} as well (see [Table 3](#)). In the case of AB stacked structures, the W-W interlayer distances increase up to ~ 6.45 Å since the interlayer W's are not on top of each other due to their stacking arrangement. On the

other hand, all the *m*-terminated geometries show increased W-W distances, and they are in the range of 6.56 – 6.84 Å (see Table 4).

It is important to note here that the increased interlayer W-W distances also correspond to their lower stacking energies as compared to the *c*-terminated geometries. Most importantly, the W-W distances are highest in the case of the AA stacked *m*-terminated heterobilayers. The increase in W-W distance weakens the van der Waals bond, which further results in lesser stability. The average intralayer W-W, W-S, and W-Se distances also play important roles in their corresponding energies. It is evident from Table 3 that all the intralayer bond distances (W-S/W-Se/W-W) are almost similar in the *c*-terminated BLs and MLs. Moreover, BLs are achieving the extra van der Waals attraction between the two layers and thus providing extreme stability. On the contrary, the intralayer W-S/W-Se distances of the *m*-terminated BLs vary a lot from their corresponding MLs and increased up to ~0.2 – 0.4 Å (see Table 4). The increase in the intralayer distance indicates the weakening of the bonds, which is in accordance with our findings. Furthermore, it is also evident from the optimized *m*-terminated MLs, that the intralayer bond length distribution varies a lot. A few bonds are shortened, and a few are elongated, resulting in a non-uniform distribution for the same. However, the interlayer bond distances are uniform in cases of all the *c*-terminated MLs and BLs.

3.2 Bader Charge Analysis of the BLs:

Bader Charge Analysis⁷⁸ is one of the well-known approximation schemes to calculate the total electronic charge around each atom within the Bader volume. We have used post analysis scripts by Henkelman group⁷⁹ to calculate the total valence electron distribution around each atom in the system. In our case, the system contains W, S, and Se, and according to our used pseudopotential, each of these atoms contain 6 valence electrons. Thus, the charge is calculated based on a total of 6 electrons. All the *c*- and *m*-terminated bilayers were considered. Electron partitioning is tabulated with their corresponding numbers in section S3 of the *SI*. The net charge on atom can be calculated as follows: a) if an atom contains less than 6 electron and the number of electrons is x (x can be a fraction too), then that atom is positively charged and the corresponding charge is $+(6-x)$ and, b) if an atom contains more than 6 electrons and the number of electrons is y (y can be a fraction too), then that atom is negatively charged and the corresponding charge is $-(y-6)$. Fig. S2 and S3 of the *SI* represent the side views of the *c*- and *m*-terminated homo/heterobilayers respectively. All atoms

are numbered (this number corresponds to the numbered atoms in the section S3 of the *SI*) and differently oriented such that most of them are visible. From the tabulated electron distribution (Section S3 of the *SI*), it is clear that all the W atoms are positively charged and all the X (S or Se) atoms are negatively charged. However, the distribution of electrons varies in a large extent for each of these systems. The variation is significant in between the *m*- and *c*-terminated systems for the homo and heterobilayers.

The highest and lowest charges on the W, S, and Se were calculated and marked with blue color inside the bracket (Section S3 of *SI*). The AA and AB stacked homobilayers show a uniform electron distribution for each W and S atoms, and it ranges in between ~3-4 electrons for W and ~6-7 electrons for S. Average electron partitions on W and S are in the range of ~3.7 and, ~6.8 respectively. On the other hand, the electron distributions show some amount of non-uniformity for the *c*-terminated AA and AB stacked heterobilayers. W attached to the S atoms show an average electron distribution in the range of ~3.7 and the W attached to the Se atoms show an average electron distribution in the range of ~4.1. As a result, the difference in electron distribution also significant in the S (higher electron distribution) and Se (lower electron distribution) atoms respectively. From our observation, it is clear that the difference in the electron distribution in heterobilayers (presence of two types of W atoms attached to different chalcogen (S/Se) atoms) as compared to the homobilayers acts as a stabilizing factor for the same. Our results suggest that the difference in electron distribution (charge separation) in between the W and X (S/Se) atoms is lower for the cases of *m*-termination and thus account for their lower negative stacking energies.

3.3 Charge Density Difference (CDD) Analysis of the BLs:

To study the underlying reason behind the difference in stability of the considered BLs, charge density distribution (CDD) analyses were performed, and the spatial distribution of the electron cloud (isosurface) was plotted. Fig 4 and 5 describe the top and side views of the CDD of the homo and hetero bilayers respectively. The homogeneous charge density distribution for the *c*-terminated homobilayers (see Fig. 4a1 and 4b1) and considerable charge density overlap between the bilayers (see Fig. 4a2 and 4b2) are in accordance with their negative stacking energy. On the other hand, the diffused electron cloud distribution in the triangular edges of the *m*-terminated homobilayers (see Fig. 4c1 and 4d1) and lesser overlap between the bilayers (see Fig. 4c2 and 4d2) strongly support their lesser negative stacking energies as compared to their *c*-terminated analogues.

However, the *c*-terminated heterobilayers show a strong electron cloud overlap between the two MLs (Fig. 5a2 and 5b2) and the extent of charge distribution in both the AA and AB stacked heterobilayers are stronger as compared to the *c*-terminated AA and AB stacked homobilayers. These findings also corroborate their corresponding stacking energy from Section 3.1 as well. Nonetheless, Fig. 5d2 is suggestive of very less electron cloud overlap in between *m*-terminated AB stacked heterobilayer and therefore, validates its lower stacking energy. Most importantly, the *m*-terminated AA stacked heterobilayer (see Fig. 5c2) does not have any charge density overlap in between the two layers, and finally turns out to be an unstable system (positive stacking energy).

3.4 Density of States (DOS) Analysis of the BLs:

To understand the changes in the electronic properties of these differently terminated bilayers, we have included the DOS analyses. The atomic DOS analyses give us an insight into the electron density distribution in or around the Fermi level, and the extent of atomic orbital overlap for each of these systems. Fig. 6 and 7 describe the partial density of states (PDOS) plot of the homo/heterobilayers. The AA/AB stacked *c*-terminated homo/heterobilayers (Fig. 6a, 6b, 7a and, 7b) show a little discontinuity in PDOS near the Fermi level (E_F) indicating semiconducting nature. However, all the *m*-terminated cases (Fig. 6c, 6d, 7c and, 7d) show continuous PDOS starting from valence to conduction level and thus strongly suggests the metallic nature. Furthermore, all the *c*-terminated homo/heterobilayers show significant overlap between the chalcogen's *p* orbitals and metal's *d* orbital below Fermi level as compared to their *m*-terminated counterparts and thus strongly suggests their extensive stability. In the case of heterobilayers, the extent of *p-d* overlap is much more significant and thus advocate towards their high stability.

From our analyses of the structural and electronic property, and the overall energetics, it clear that both *c*-terminated homo/hetero BLs are more likely to exist as bilayer 2D TMD growth products. The absence of structural deformity, homogeneous charge, and electron cloud distribution combine to form the most stable *c*-terminated geometries. Among *m*-terminated homo BLs, both the AA and AB stacking seems to be stable and are likely to exist, although, they are less stable than their *c*-terminated analogues. On the contrary, the AA stacked *m*-terminated BL is most likely to be non-existent. The instability or the lesser stability of the *m*-terminated cases can be due to the presence of dangling bonds (unsatisfied valence) of the heavy transition metal W. Due to W-

termination, their valency is not satisfied fully and thus leading towards the structural instability. Our study explores three different aspects such as a) the effect of edge termination, b) the effect of different stacking, and c) the comparison of homo and hetero bilayers and draws an insightful picture for the probability of their existence as a bilayer TMD growth product. This study gives a motivation towards the controlled growth process of the homo and hetero layered TMDs and aims to provide a clear path towards the application-dependent TMD synthesis.

4. Conclusion

In this DFT based study, electronic insights of the controlled bilayer TMD growth products with the changing parameters were studied. Three main parameters were considered such as different edge termination (*c*- and *m*- terminated), different bilayer stacking (AA and AB), and the change in the chalcogen atoms in one of the layers (homo and hetero). Tungsten (W) based chalcogenides (S and Se) were chosen due to their increasing demand in electronic applications over the well-studied Mo based systems. Any applications of these 2D Tungsten Chalcogenides (WX₂) require a well-established controlled synthesis path due to their structural dependent applications. Formation of bilayer flakes of these chalcogenides is a major research area and our calculation suggests the extreme stability of the *c*-terminated cases over the *m*-terminated bilayer growth products for both the homo and heterobilayers. The experimental detection method of presence/absence of particular growth products and their particular ratio in the reaction vessel is very difficult and sometimes results in erroneous prediction. However, this benchmarking computational study draws a clear picture in terms of the bilayer growth products based on the energetics and electronics to achieve an application based controlled bilayer TMD products. Although this study only gives an assessment based on the three most well contributed parameters, more parameters can also be added, and it is currently under investigation.

Acknowledgement

This work was supported in part by National Science Foundation award (ECCS-1104870), the Defense University Research Instrumentation Program (FA9550-11-1-0272), and the NJIT faculty start-up grant. We are grateful to the High- Performance Computing (HPC) facilities managed by Academic and Research Computing Systems (ARCS) in the Department of Information Services

and Technology (IST) of the New Jersey Institute of Technology (NJIT). Some computations were performed on Kong.njit.edu HPC cluster, managed by ARCS. We acknowledge the support of the Extreme Science and Engineering Discovery Environment (XSEDE) for providing us their computational facilities (Start Up Allocation – DMR170065 & Research Allocation – DMR180013).

Data Availability

The datasets generated during and/or analyzed during the current study are available from the corresponding author on reasonable request.

Competing Interests

The authors declare that there are no competing interests.

Author Contribution

All authors contributed to designing the project. KG performed all the calculations and discussed results with DD, KK, and EH. KG wrote the manuscript. All authors checked the final draft.

References

- 1 Schwierz, F. Graphene Transistors: Status, Prospects, and Problems. *Proceedings of the IEEE* **101**, 1567-1584, doi:10.1109/JPROC.2013.2257633 (2013).
- 2 Novoselov, K. S. *et al.* Electric Field Effect in Atomically Thin Carbon Films. *Science* **306**, 666, doi:10.1126/science.1102896 (2004).
- 3 Wang, Q. H., Kalantar-Zadeh, K., Kis, A., Coleman, J. N. & Strano, M. S. Electronics and optoelectronics of two-dimensional transition metal dichalcogenides. *Nature nanotechnology* **7**, 699-712 (2012).
- 4 Butler, S. Z. *et al.* Progress, challenges, and opportunities in two-dimensional materials beyond graphene. *ACS nano* **7**, 2898-2926 (2013).
- 5 Xu, M., Liang, T., Shi, M. & Chen, H. Graphene-like two-dimensional materials. *Chemical reviews* **113**, 3766-3798 (2013).
- 6 Geim, A. K. & Grigorieva, I. V. Van der Waals heterostructures. *Nature* **499**, 419, doi:10.1038/nature12385 (2013).
- 7 Manzeli, S., Ovchinnikov, D., Pasquier, D., Yazyev, O. V. & Kis, A. 2D transition metal dichalcogenides. *Nature Reviews Materials* **2**, 17033, doi:10.1038/natrevmats.2017.33 (2017).
- 8 Mak, K. F. & Shan, J. Photonics and optoelectronics of 2D semiconductor transition metal dichalcogenides. *Nature Photonics* **10**, 216, doi:10.1038/nphoton.2015.282 (2016).

- 9 Li, Z., Meng, X. & Zhang, Z. Recent development on MoS₂-based photocatalysis: A review. *Journal of Photochemistry and Photobiology C: Photochemistry Reviews* **35**, 39-55, doi:<https://doi.org/10.1016/j.jphotochemrev.2017.12.002> (2018).
- 10 Jariwala, D., Sangwan, V. K., Lauhon, L. J., Marks, T. J. & Hersam, M. C. Emerging Device Applications for Semiconducting Two-Dimensional Transition Metal Dichalcogenides. *ACS Nano* **8**, 1102-1120, doi:10.1021/nn500064s (2014).
- 11 Chhowalla, M. *et al.* The chemistry of two-dimensional layered transition metal dichalcogenide nanosheets. *Nature Chemistry* **5**, 263, doi:10.1038/nchem.1589 (2013).
- 12 Mak, K. F., Lee, C., Hone, J., Shan, J. & Heinz, T. F. Atomically Thin $\{\mathrm{MoS}\}_2$: A New Direct-Gap Semiconductor. *Physical Review Letters* **105**, 136805, doi:10.1103/PhysRevLett.105.136805 (2010).
- 13 Radisavljevic, B., Radenovic, A., Brivio, J., Giacometti, V. & Kis, A. Single-layer MoS₂ transistors. *Nature Nanotechnology* **6**, 147, doi:10.1038/nnano.2010.279 <https://www.nature.com/articles/nnano.2010.279#supplementary-information> (2011).
- 14 Splendiani, A. *et al.* Emerging Photoluminescence in Monolayer MoS₂. *Nano Letters* **10**, 1271-1275, doi:10.1021/nl903868w (2010).
- 15 Dankert, A., Langouche, L., Kamalakar, M. V. & Dash, S. P. High-Performance Molybdenum Disulfide Field-Effect Transistors with Spin Tunnel Contacts. *ACS Nano* **8**, 476-482, doi:10.1021/nn404961e (2014).
- 16 Zeng, H., Dai, J., Yao, W., Xiao, D. & Cui, X. Valley polarization in MoS₂ monolayers by optical pumping. *Nature Nanotechnology* **7**, 490, doi:10.1038/nnano.2012.95 <https://www.nature.com/articles/nnano.2012.95#supplementary-information> (2012).
- 17 Gaur, A. P. S. *et al.* Surface Energy Engineering for Tunable Wettability through Controlled Synthesis of MoS₂. *Nano Letters* **14**, 4314-4321, doi:10.1021/nl501106v (2014).
- 18 Xu, X., Yao, W., Xiao, D. & Heinz, T. F. Spin and pseudospins in layered transition metal dichalcogenides. *Nature Physics* **10**, 343-350 (2014).
- 19 Gaur, A. P. S., Sahoo, S., Scott, J. F. & Katiyar, R. S. Electron-Phonon Interaction and Double-Resonance Raman Studies in Monolayer WS₂. *The Journal of Physical Chemistry C* **119**, 5146-5151, doi:10.1021/jp512540u (2015).
- 20 Gutiérrez, H. R. *et al.* Extraordinary Room-Temperature Photoluminescence in Triangular WS₂ Monolayers. *Nano Letters* **13**, 3447-3454, doi:10.1021/nl3026357 (2013).
- 21 Chen, J. *et al.* Synthesis of Wafer-Scale Monolayer WS₂ Crystals toward the Application in Integrated Electronic Devices. *ACS Applied Materials & Interfaces* **11**, 19381-19387, doi:10.1021/acsami.9b04791 (2019).
- 22 Zhu, Z. Y., Cheng, Y. C. & Schwingenschlögl, U. Giant spin-orbit-induced spin splitting in two-dimensional transition-metal dichalcogenide semiconductors. *Physical Review B* **84**, 153402, doi:10.1103/PhysRevB.84.153402 (2011).
- 23 Liu, L., Kumar, S. B., Ouyang, Y. & Guo, J. Performance Limits of Monolayer Transition Metal Dichalcogenide Transistors. *IEEE Transactions on Electron Devices* **58**, 3042-3047, doi:10.1109/TED.2011.2159221 (2011).
- 24 Coleman, J. N. *et al.* Two-Dimensional Nanosheets Produced by Liquid Exfoliation of Layered Materials. *Science* **331**, 568, doi:10.1126/science.1194975 (2011).
- 25 Zeng, Z. *et al.* Single-Layer Semiconducting Nanosheets: High-Yield Preparation and Device Fabrication. *Angewandte Chemie* **123**, 11289-11293, doi:10.1002/ange.201106004 (2011).
- 26 Voiry, D. *et al.* Enhanced catalytic activity in strained chemically exfoliated WS₂ nanosheets for hydrogen evolution. *Nature Materials* **12**, 850, doi:10.1038/nmat3700

<https://www.nature.com/articles/nmat3700#supplementary-information> (2013).

- 27 Ramakrishna Matte, H. S. S. *et al.* MoS₂ and WS₂ Analogues of Graphene. *Angewandte Chemie International Edition* **49**, 4059-4062, doi:10.1002/anie.201000009 (2010).
- 28 Muratore, C. *et al.* Continuous ultra-thin MoS₂ films grown by low-temperature physical vapor deposition. *Applied Physics Letters* **104**, 261604, doi:10.1063/1.4885391 (2014).
- 29 Gong, C. *et al.* Metal Contacts on Physical Vapor Deposited Monolayer MoS₂. *ACS Nano* **7**, 11350-11357, doi:10.1021/nn4052138 (2013).
- 30 Le Mogne, T. *et al.* Nature of super-lubricating MoS₂ physical vapor deposition coatings. *Journal of Vacuum Science & Technology A* **12**, 1998-2004, doi:10.1116/1.578996 (1994).
- 31 Lee, Y.-H. *et al.* Synthesis of Large-Area MoS₂ Atomic Layers with Chemical Vapor Deposition. *Advanced Materials* **24**, 2320-2325, doi:10.1002/adma.201104798 (2012).
- 32 Wang, X., Feng, H., Wu, Y. & Jiao, L. Controlled Synthesis of Highly Crystalline MoS₂ Flakes by Chemical Vapor Deposition. *Journal of the American Chemical Society* **135**, 5304-5307, doi:10.1021/ja4013485 (2013).
- 33 Li, Y. *et al.* Leaf-Like V₂O₅ Nanosheets Fabricated by a Facile Green Approach as High Energy Cathode Material for Lithium-Ion Batteries. *Advanced Energy Materials* **3**, 1171-1175, doi:10.1002/aenm.201300188 (2013).
- 34 Lee, Y.-H. *et al.* Synthesis and Transfer of Single-Layer Transition Metal Disulfides on Diverse Surfaces. *Nano Letters* **13**, 1852-1857, doi:10.1021/nl400687n (2013).
- 35 Kobayashi, Y. *et al.* Growth and Optical Properties of High-Quality Monolayer WS₂ on Graphite. *ACS Nano* **9**, 4056-4063, doi:10.1021/acsnano.5b00103 (2015).
- 36 Zhang, Y. *et al.* Chemical vapor deposition of monolayer WS₂ nanosheets on Au foils toward direct application in hydrogen evolution. *Nano Research* **8**, 2881-2890, doi:10.1007/s12274-015-0793-z (2015).
- 37 Chow, P. K. *et al.* Wetting of Mono and Few-Layered WS₂ and MoS₂ Films Supported on Si/SiO₂ Substrates. *ACS Nano* **9**, 3023-3031, doi:10.1021/nn5072073 (2015).
- 38 Zhan, Y., Liu, Z., Najmaei, S., Ajayan, P. M. & Lou, J. Large-Area Vapor-Phase Growth and Characterization of MoS₂ Atomic Layers on a SiO₂ Substrate. *Small* **8**, 966-971, doi:10.1002/smll.201102654 (2012).
- 39 Okada, M. *et al.* Direct Chemical Vapor Deposition Growth of WS₂ Atomic Layers on Hexagonal Boron Nitride. *ACS Nano* **8**, 8273-8277, doi:10.1021/nn503093k (2014).
- 40 Emtsev, K. V. *et al.* Towards wafer-size graphene layers by atmospheric pressure graphitization of silicon carbide. *Nature materials* **8**, 203-207 (2009).
- 41 Tanabe, S., Sekine, Y., Kageshima, H., Nagase, M. & Hibino, H. Carrier transport mechanism in graphene on SiC (0001). *Physical Review B* **84**, 115458 (2011).
- 42 Jobst, J. *et al.* Quantum oscillations and quantum Hall effect in epitaxial graphene. *Physical Review B* **81**, 195434 (2010).
- 43 Koma, A. & Yoshimura, K. Ultrasharp interfaces grown with Van der Waals epitaxy. *Surface Science* **174**, 556-560 (1986).
- 44 Koma, A. Van der Waals epitaxy for highly lattice-mismatched systems. *Journal of crystal growth* **201**, 236-241 (1999).
- 45 Van Der Zande, A. M. *et al.* Grains and grain boundaries in highly crystalline monolayer molybdenum disulphide. *Nature materials* **12**, 554-561 (2013).
- 46 Zhang, W., Wang, Q., Chen, Y., Wang, Z. & Wee, A. T. S. Van der Waals stacked 2D layered materials for optoelectronics. *2D Materials* **3**, 022001, doi:10.1088/2053-1583/3/2/022001 (2016).
- 47 Zhang, K. *et al.* Interlayer transition and infrared photodetection in atomically thin type-II MoTe₂/MoS₂ van der Waals heterostructures. *ACS nano* **10**, 3852-3858 (2016).

- 48 Amin, B., Singh, N. & Schwingenschlögl, U. Heterostructures of transition metal dichalcogenides. *Physical Review B* **92**, 075439, doi:10.1103/PhysRevB.92.075439 (2015).
- 49 Zhu, H. L. *et al.* Evolution of band structures in MoS₂-based homo- and heterobilayers. *Journal of Physics D: Applied Physics* **49**, 065304, doi:10.1088/0022-3727/49/6/065304 (2016).
- 50 Terrones, H., López-Urías, F. & Terrones, M. Novel hetero-layered materials with tunable direct band gaps by sandwiching different metal disulfides and diselenides. *Scientific Reports* **3**, 1549, doi:10.1038/srep01549
- <https://www.nature.com/articles/srep01549#supplementary-information> (2013).
- 51 Zhang, C. *et al.* Interlayer couplings, Moiré patterns, and 2D electronic superlattices in MoS₂/WSe₂ hetero-bilayers. *Science Advances* **3**, e1601459, doi:10.1126/sciadv.1601459 (2017).
- 52 Hsu, W.-T. *et al.* Second Harmonic Generation from Artificially Stacked Transition Metal Dichalcogenide Twisted Bilayers. *ACS Nano* **8**, 2951-2958, doi:10.1021/nn500228r (2014).
- 53 Wang, K. *et al.* Interlayer Coupling in Twisted WSe₂/WS₂ Bilayer Heterostructures Revealed by Optical Spectroscopy. *ACS Nano* **10**, 6612-6622, doi:10.1021/acsnano.6b01486 (2016).
- 54 Peimyoo, N. *et al.* Nonblinking, Intense Two-Dimensional Light Emitter: Monolayer WS₂ Triangles. *ACS Nano* **7**, 10985-10994, doi:10.1021/nn4046002 (2013).
- 55 Kresse, G. & Furthmüller, J. Efficient iterative schemes for ab initio total-energy calculations using a plane-wave basis set. *Physical review B* **54**, 11169 (1996).
- 56 Blöchl, P. E. Projector augmented-wave method. *Physical review B* **50**, 17953 (1994).
- 57 Kresse, G. & Joubert, D. From ultrasoft pseudopotentials to the projector augmented-wave method. *Physical Review B* **59**, 1758 (1999).
- 58 Perdew, J. P., Burke, K. & Ernzerhof, M. Generalized Gradient Approximation Made Simple. *Physical Review Letters* **77**, 3865-3868, doi:10.1103/PhysRevLett.77.3865 (1996).
- 59 Klimeš, J., Bowler, D. R. & Michaelides, A. Chemical accuracy for the van der Waals density functional. *Journal of Physics: Condensed Matter* **22**, 022201, doi:10.1088/0953-8984/22/2/022201 (2009).
- 60 Klimeš, J., Bowler, D. R. & Michaelides, A. Van der Waals density functionals applied to solids. *Physical Review B* **83**, 195131, doi:10.1103/PhysRevB.83.195131 (2011).
- 61 Klimeš, J. & Michaelides, A. Perspective: Advances and challenges in treating van der Waals dispersion forces in density functional theory. *The Journal of Chemical Physics* **137**, 120901, doi:10.1063/1.4754130 (2012).
- 62 Ramasubramaniam, A., Naveh, D. & Towe, E. Tunable band gaps in bilayer transition-metal dichalcogenides. *Physical Review B* **84**, 205325, doi:10.1103/PhysRevB.84.205325 (2011).
- 63 Bhattacharyya, S. & Singh, A. K. Semiconductor-metal transition in semiconducting bilayer sheets of transition-metal dichalcogenides. *Physical Review B* **86**, 075454, doi:10.1103/PhysRevB.86.075454 (2012).
- 64 Chen, Q. *et al.* Atomically Flat Zigzag Edges in Monolayer MoS₂ by Thermal Annealing. *Nano Letters* **17**, 5502-5507, doi:10.1021/acs.nanolett.7b02192 (2017).
- 65 Bollinger, M., Jacobsen, K. & Nørskov, J. *Phys. Rev. B: Condens. Matter Mater. Phys.* **67**, 85410 (2003).
- 66 Helveg, S. *et al.* Atomic-Scale Structure of Single-Layer MoS_2 Nanoclusters. *Physical Review Letters* **84**, 951-954, doi:10.1103/PhysRevLett.84.951 (2000).
- 67 Gibertini, M. & Marzari, N. Emergence of One-Dimensional Wires of Free Carriers in Transition-Metal-Dichalcogenide Nanostructures. *Nano Letters* **15**, 6229-6238, doi:10.1021/acs.nanolett.5b02834 (2015).

- 68 Li, Y., Zhou, Z., Zhang, S. & Chen, Z. MoS₂ Nanoribbons: High Stability and Unusual Electronic and Magnetic Properties. *Journal of the American Chemical Society* **130**, 16739-16744, doi:10.1021/ja805545x (2008).
- 69 Bollinger, M. V. *et al.* One-Dimensional Metallic Edge States in MoS_2 . *Physical Review Letters* **87**, 196803, doi:10.1103/PhysRevLett.87.196803 (2001).
- 70 Xiao, S.-L., Yu, W.-Z. & Gao, S.-P. Edge preference and band gap characters of MoS₂ and WS₂ nanoribbons. *Surface Science* **653**, 107-112, doi:<https://doi.org/10.1016/j.susc.2016.06.011> (2016).
- 71 Lauritsen, J. V. *et al.* Size-dependent structure of MoS₂ nanocrystals. *Nature Nanotechnology* **2**, 53, doi:10.1038/nnano.2006.171 (2007).
- 72 Schweiger, H., Raybaud, P., Kresse, G. & Toulhoat, H. Shape and Edge Sites Modifications of MoS₂ Catalytic Nanoparticles Induced by Working Conditions: A Theoretical Study. *Journal of Catalysis* **207**, 76-87, doi:<https://doi.org/10.1006/jcat.2002.3508> (2002).
- 73 Li, S. *et al.* Halide-assisted atmospheric pressure growth of large WSe₂ and WS₂ monolayer crystals. *Applied Materials Today* **1**, 60-66, doi:<https://doi.org/10.1016/j.apmt.2015.09.001> (2015).
- 74 Liu, H. *et al.* Fluorescence Concentric Triangles: A Case of Chemical Heterogeneity in WS₂ Atomic Monolayer. *Nano Letters* **16**, 5559-5567, doi:10.1021/acs.nanolett.6b02111 (2016).
- 75 Yang, S. Y., Shim, G. W., Seo, S.-B. & Choi, S.-Y. Effective shape-controlled growth of monolayer MoS₂ flakes by powder-based chemical vapor deposition. *Nano Research* **10**, 255-262, doi:10.1007/s12274-016-1284-6 (2017).
- 76 Zobel, A. *et al.* Chemical vapour deposition and characterization of uniform bilayer and trilayer MoS₂ crystals. *Journal of Materials Chemistry C* **4**, 11081-11087, doi:10.1039/C6TC03587F (2016).
- 77 Han, A. *et al.* Growth of 2H stacked WSe₂ bilayers on sapphire. *Nanoscale Horizons*, doi:10.1039/C9NH00260J (2019).
- 78 Bader, R. F. W. A quantum theory of molecular structure and its applications. *Chemical Reviews* **91**, 893-928, doi:10.1021/cr00005a013 (1991).
- 79 Group, H. <http://theory.cm.utexas.edu/henkelman/code/bader/>.

Tables

Controlled edge dependent stacking of WS₂-WS₂ Homo- and WS₂-WSe₂ Hetero-structures: A Computational Study

Kamalika Ghatak¹, Kyung Nam Kang², Eui-Hyeok Yang*², Dibakar Datta*¹

¹ Department of Mechanical and Industrial Engineering, New Jersey Institute of Technology, Newark, NJ 07103, USA

² Department of Mechanical Engineering, Stevens Institute of Technology, Hoboken, NJ 07030, USA

* Corresponding author

Table 1. Stacking energies of different edged and differently stacked homobilayers.

Species	ΔG_f (eV)
AA stacked <i>c</i> -terminated homobilayer	-1.8076437
AB stacked <i>c</i> -terminated homobilayer	-1.92999697
AA stacked <i>m</i> -terminated homobilayer	-0.3802691
AA stacked <i>m</i> -terminated homobilayer	-0.1542134

Table 2. Stacking energies of different edged and differently stacked heterobilayers.

Species	ΔG_f (eV)
AA stacked <i>c</i> -terminated heterobilayer	-2.64495617
AB stacked <i>c</i> -terminated heterobilayer	-1.90643926
AA stacked <i>m</i> -terminated heterobilayer	0.83085255
AB stacked <i>m</i> -terminated heterobilayer	-0.31549407

Table 3. Average bond distances of intralayer W-S, W-W, and interlayer W-W of *c*-terminated MLs and BLs.

Species	Avg. W-S (Å)	Avg. W-Se (Å)	Avg. Intra W-W (Å)	Avg. Inter W-W (Å)
WS ₂ <i>c</i> -terminated	2.413018571	--	3.161553333	--
WSe ₂ <i>c</i> -terminated	--	2.613228571	3.244215	--
WS ₂ -WS ₂ AA stacked <i>c</i> -terminated	2.416548889	--	3.153309091	6.28111875
WS ₂ -WS ₂ AB stacked <i>c</i> -terminated	2.404327778	--	3.137748182	6.455065
WS ₂ -WSe ₂ AA stacked <i>c</i> -terminated	2.416011667	2.509388333	3.188602727	6.25176625
WS ₂ -WSe ₂ AB stacked <i>c</i> -terminated	2.414475	2.52706	3.171012727	6.45871125

Table 4. Average bond distances of intralayer W-S, W-W, and interlayer W-W of *m*-terminated MLs and BLs.

Species	Avg. W-S (Å)	Avg. W-Se (Å)	Avg. Intra W-W (Å)	Avg. Inter W-W (Å)
WS ₂ <i>m</i> -terminated	2.412232857	--	2.906161667	--
WSe ₂ <i>m</i> -terminated	--	2.50215	2.978058333	--
WS ₂ -WS ₂ AA stacked <i>m</i> -terminated	2.390242222	--	2.870407273	6.58096125
WS ₂ -WS ₂ AB stacked <i>m</i> -terminated	2.380716667	--	2.896436364	6.56902375
WS ₂ -WSe ₂ AA stacked <i>m</i> -terminated	2.507915	2.95827	3.186575	6.8431425
WS ₂ -WSe ₂ AB stacked <i>m</i> -terminated	2.519025	2.61946	3.136821667	6.6746925

Figures

Controlled edge dependent stacking of WS₂-WS₂ Homo- and WS₂-WSe₂ Hetero-structures: A Computational Study

Kamalika Ghatak¹, Kyung Nam Kang², Eui-Hyeok Yang^{2,*}, Dibakar Datta^{1,*}

¹ Department of Mechanical and Industrial Engineering, New Jersey Institute of Technology, Newark, NJ 07103, USA

² Department of Mechanical Engineering, Stevens Institute of Technology, Hoboken, NJ 07030, USA

* Corresponding author

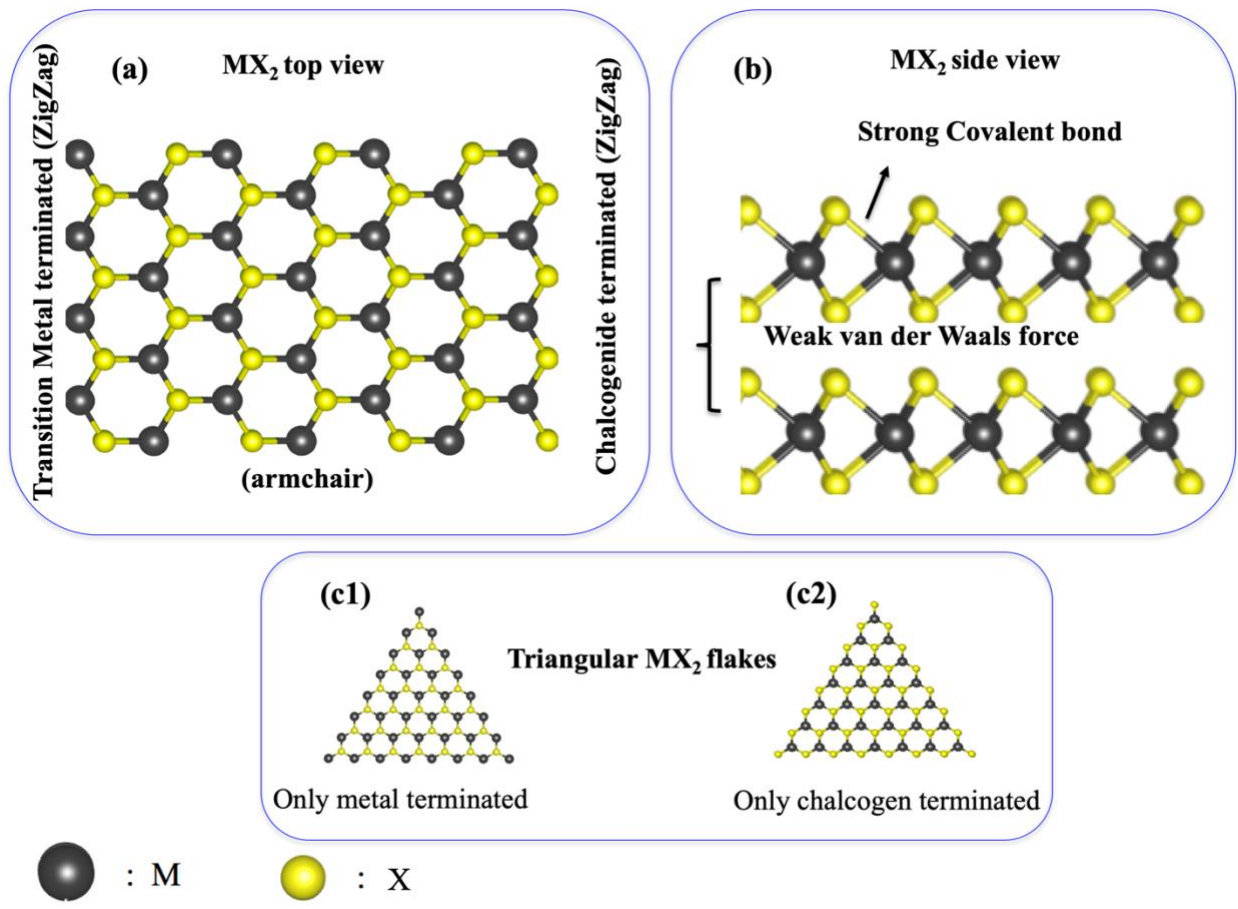


Figure 1. General structural features of 2D- MX_2 (a) Top view of 2D- MX_2 , (b) side view of a bilayer 2D- MX_2 , (c) triangular MX_2 metal/chalcogen terminated zigzag edged structures.

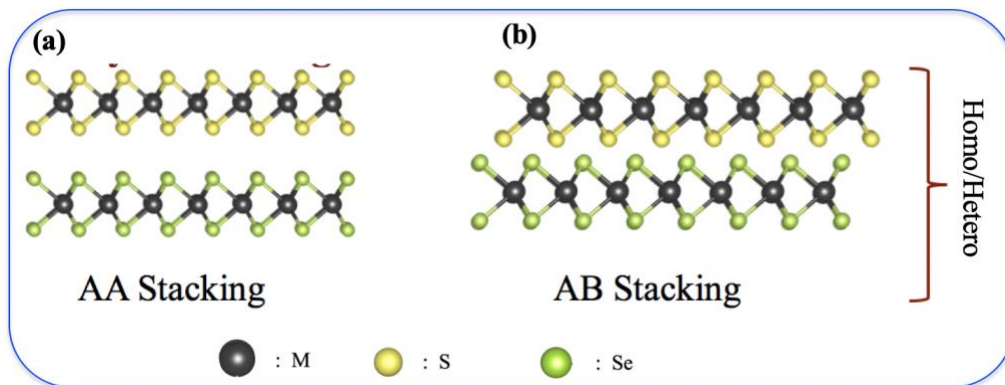


Figure 2. General structural features of 2D-stacked MX₂ bilayers (a) AA stacking, (b) AB stacking.

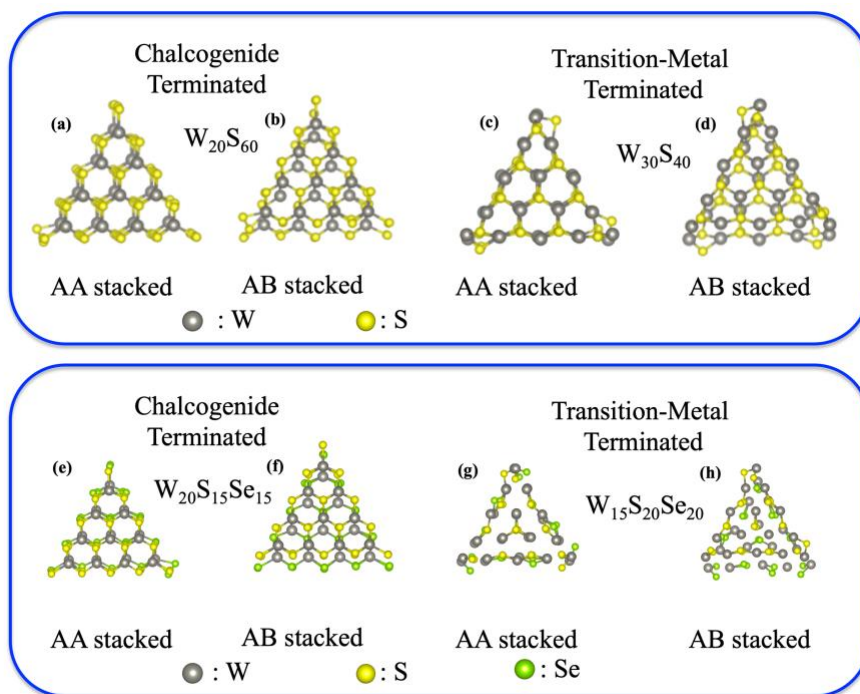


Figure 3. Optimized structures of 2D-stacked MX₂ bilayers (a) *c*-terminated AA stacked homo bilayer, (b) *c*-terminated AB stacked homo bilayer, (c) *m*-terminated AA stacked homo bilayer, (d) *m*-terminated AB stacked homo bilayer, (e) *c*-terminated AA stacked hetero bilayer, (f) *c*-terminated AB stacked hetero bilayer, (g) *m*-terminated AA stacked hetero bilayer, (h) *m*-terminated AB stacked hetero bilayer.

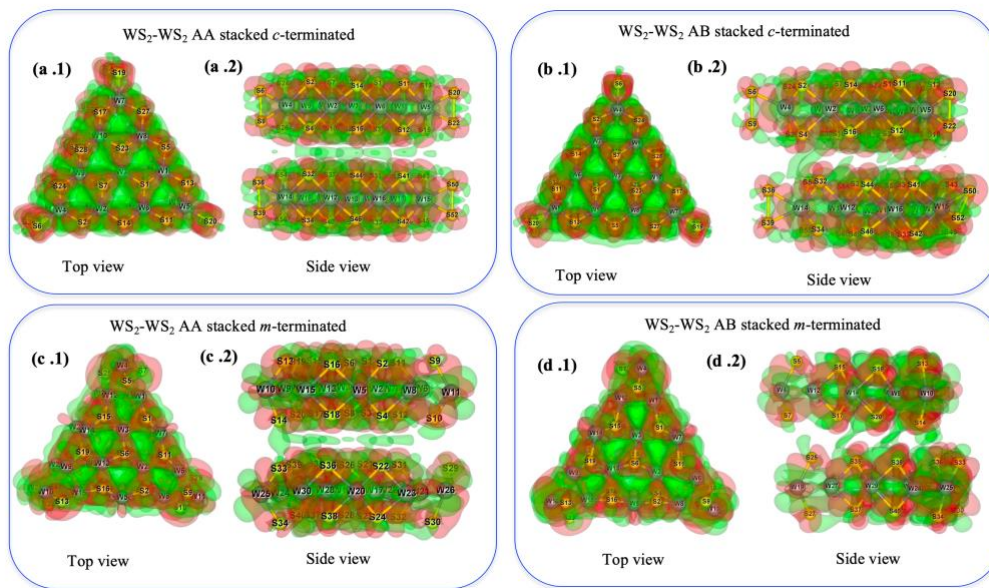


Figure 4. CDD plot of 2D-stacked MX₂ bilayers (a) *c*-terminated AA stacked homobilayer, (b) *c*-terminated AB stacked homobilayer, (c) *m*-terminated AA stacked homobilayer, (d) *m*-terminated AB stacked homobilayer.

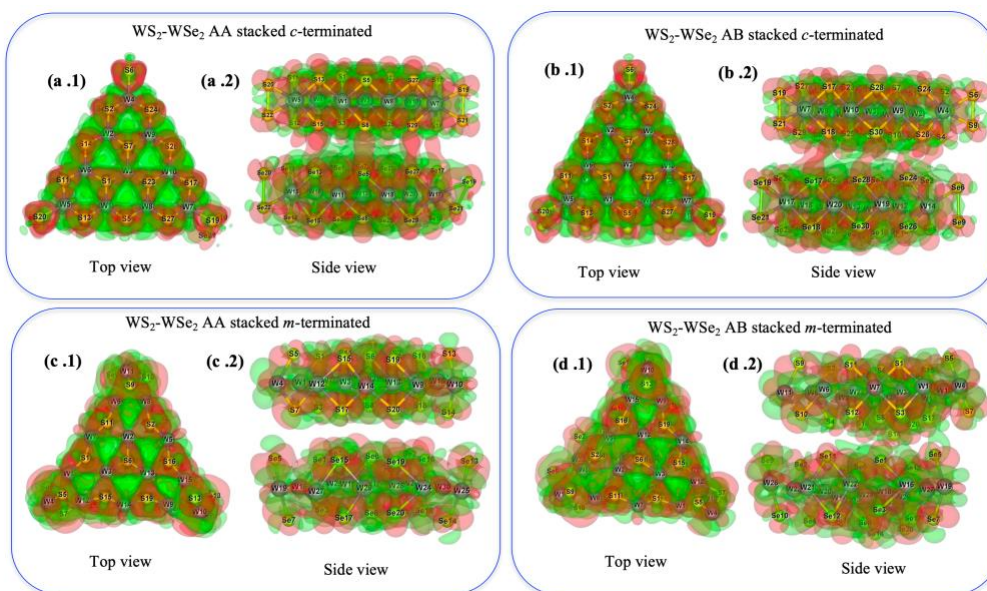


Figure 5. CDD plot of 2D-stacked MX₂ bilayers (a) *c*-terminated AA stacked heterobilayer, (b) *c*-terminated AB stacked heterobilayer, (c) *m*-terminated AA stacked heterobilayer, (d) *m*-terminated AB stacked heterobilayer.

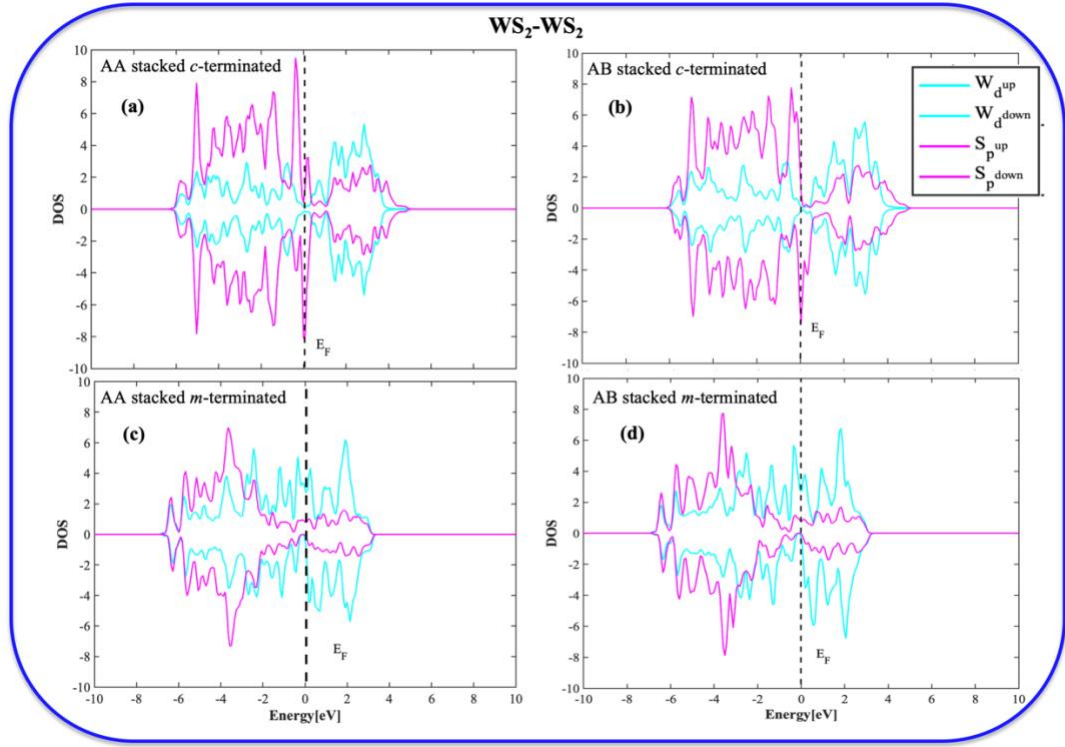


Figure 6. Partial Density of States (PDOS) plots of (a) *c*-terminated AA stacked homobilayer, (b) *c*-terminated AB stacked homobilayer, (c) *m*-terminated AA stacked homobilayer, (d) *m*-terminated AB stacked homobilayer.

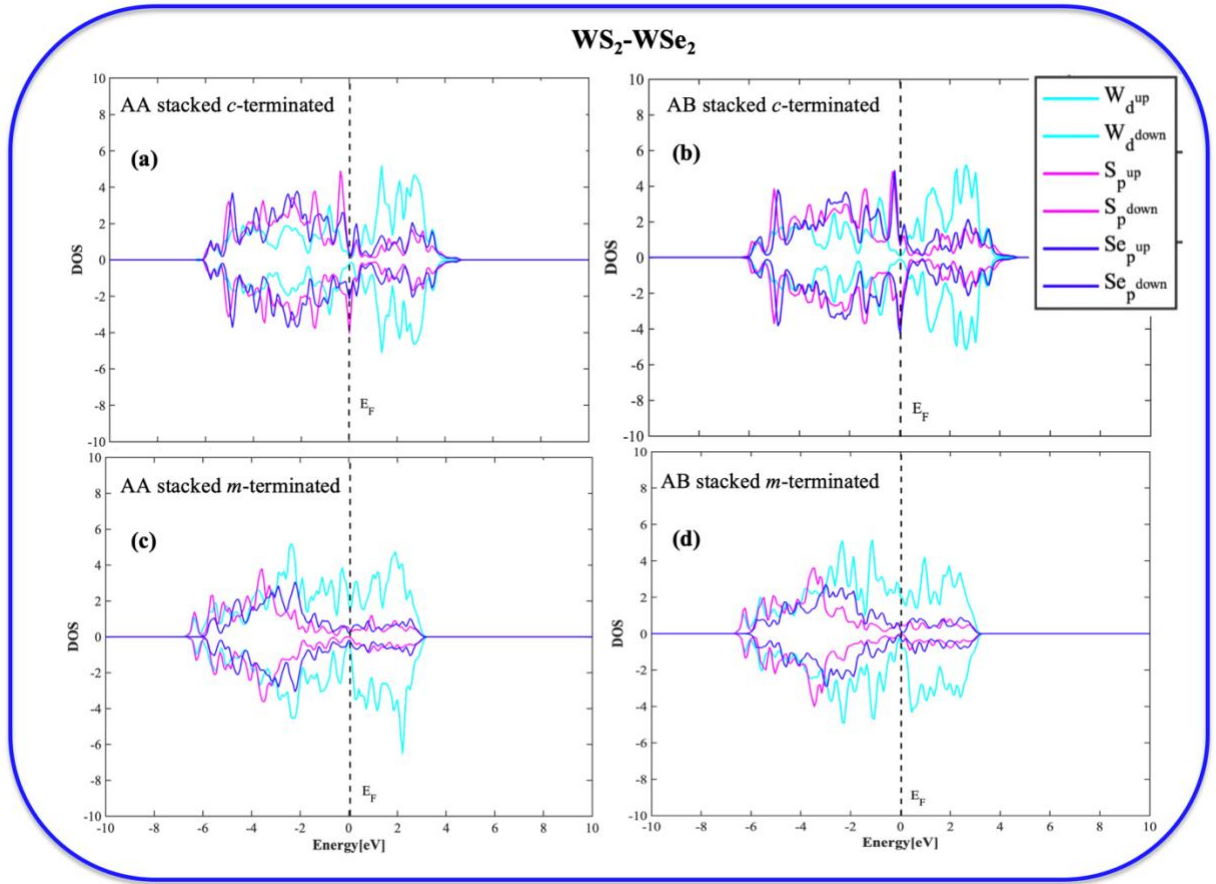


Figure 7. Partial Density of States (PDOS) plots of (a) *c*-terminated AA stacked heterobilayer, (b) *c*-terminated AB stacked heterobilayer, (c) *m*-terminated AA stacked heterobilayer, (d) *m*-terminated AB stacked heterobilayer.

Supporting Information

Controlled edge dependent stacking of WS₂-WS₂ Homo- and WS₂-WSe₂ Hetero-structures: A Computational Study

Kamalika Ghatak¹, Kyung Nam Kang², Eui-Hyeok Yang^{2,*}, Dibakar Datta^{1,*}

¹ Department of Mechanical and Industrial Engineering, New Jersey Institute of Technology, Newark, NJ 07103, USA

² Department of Mechanical Engineering, Stevens Institute of Technology, Hoboken, NJ 07030, USA

* Corresponding author

Section S1. Scaling of the calculation setup (VASP):

All our structures are non-periodic in nature, and therefore, it requires the increased simulation box size to avoid the error due to the periodic image overlap. We have utilized GPU facility of our institutional cluster KONG for VASP simulation. To scale the kinetic energy cut-off, we have considered one case with a total of 80 atoms (BL-c-AA-W₂₀S₆₀). For this case, a box size of (35× 35×35) Å with 4 combinations of energy cut-off starting from 300-600 eV (300, 400, 500, and 600 eV) were taken. We have performed 4 single point calculation, and the variation in energy values from 400 eV – 600 eV is insignificant. Therefore, we have considered 400 eV kinetic energy cut-off for all our computations. Moreover, this single point calculation (one geometric iteration) takes time in between ~2-3 hrs. and the time increases with the increasing kinetic cut-off values. These number of geometric iterations for all these structures vary in between ~200-400 geometric iterations depending upon the systems. There are few reasons behind this significant time requirement for all these geometries: a) the presence of heavy transition metal such as

W, b) the huge box size, c) high kinetic energy cut-off and, finally d) the non-periodic nature of the calculation. Therefore, an optimized combination of all these issues need to be taken care of in order to resist the huge computational cost. In this regard, we first considered 2 combinations of the cubic cell sizes Comb-A ($35 \times 35 \times 35$) Å³ and, Comb-B ($27 \times 27 \times 27$) Å³ and ran a single point calculation to trace the time consumption (row 1 and 2 of Table 1). In these two cases, the average wall time/ iteration is huge, and it will take a lot of time in order to get the full optimization. Therefore, after several trials and error, we have optimized the simulation box size to be Comb-C ($24 \times 22 \times 20$) Å³ (row 3 of Table S1), where the distance of the two consecutive periodic images were kept more than 8 Å. The initial lengths of the triangular *c*-terminated and *m*-terminated flakes are ~ 13.2 Å, and ~ 11.8 Å.

Table S1. Cell size parametrization for TMD BL optimization.

Species	Stacking	Energy Cutoff	Cell size	Per iteration average time in hrs.
BL c-W ₂₀ S ₆₀ (Single point)	AA	400	35× 35×35 (comb-A)	2.10
BL c-W ₂₀ S ₆₀ (Single point)	AA	400	27× 27×27 (comb-B)	1.29
BL c-W ₂₀ S ₆₀ (Optimized)	AA	400	24× 22×20 (comb-C)	0.31

Section S2. Labelled optimized geometries of the ML & BL TMDs:

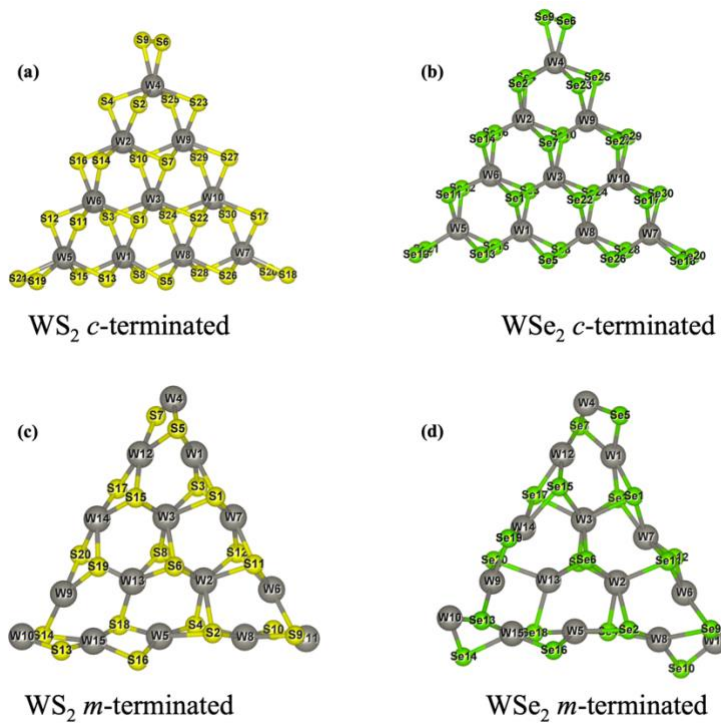


Fig. S1. Optimized labelled top views of a) *c*-terminated WS_2 , b) *c*-terminated WSe_2 , c) *m*-terminated WS_2 and, d) *m*-terminated WSe_2 .

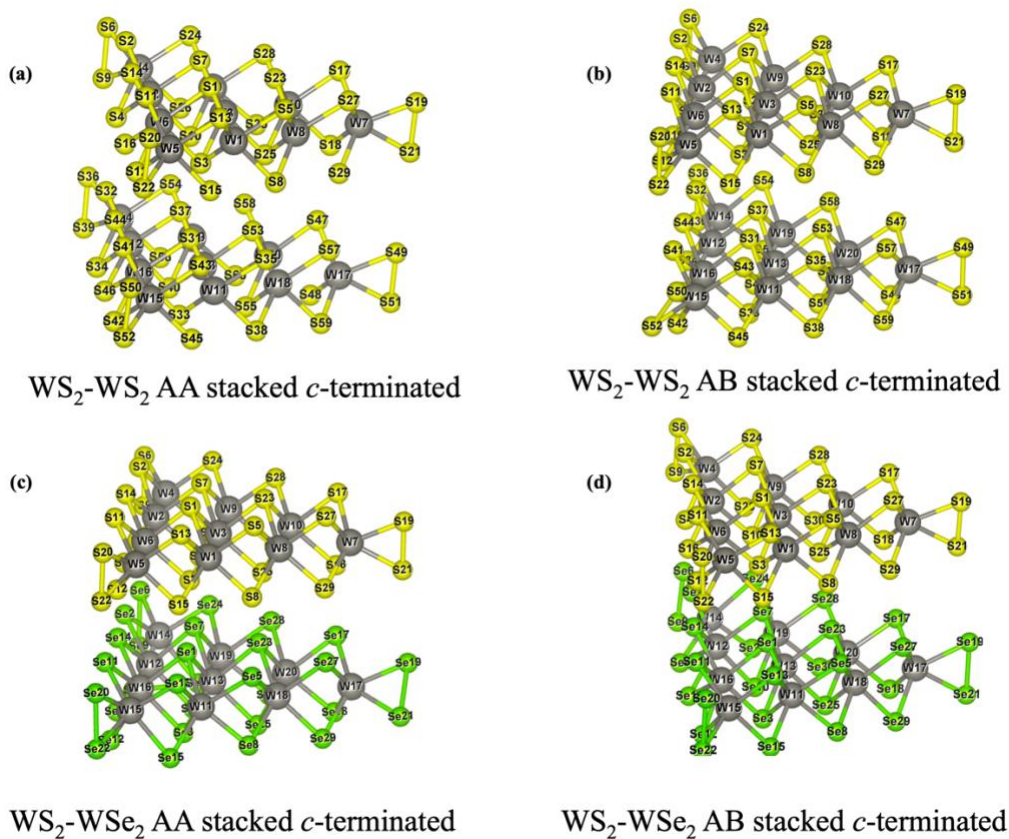


Fig. S2. Optimized labelled side views of a) *c*-terminated AA stacked WS_2 - WS_2 , b) *c*-terminated AB stacked WS_2 - WS_2 , c) *c*-terminated AA stacked WS_2 - WSe_2 and, d) *c*-terminated AB stacked WS_2 - WSe_2 .

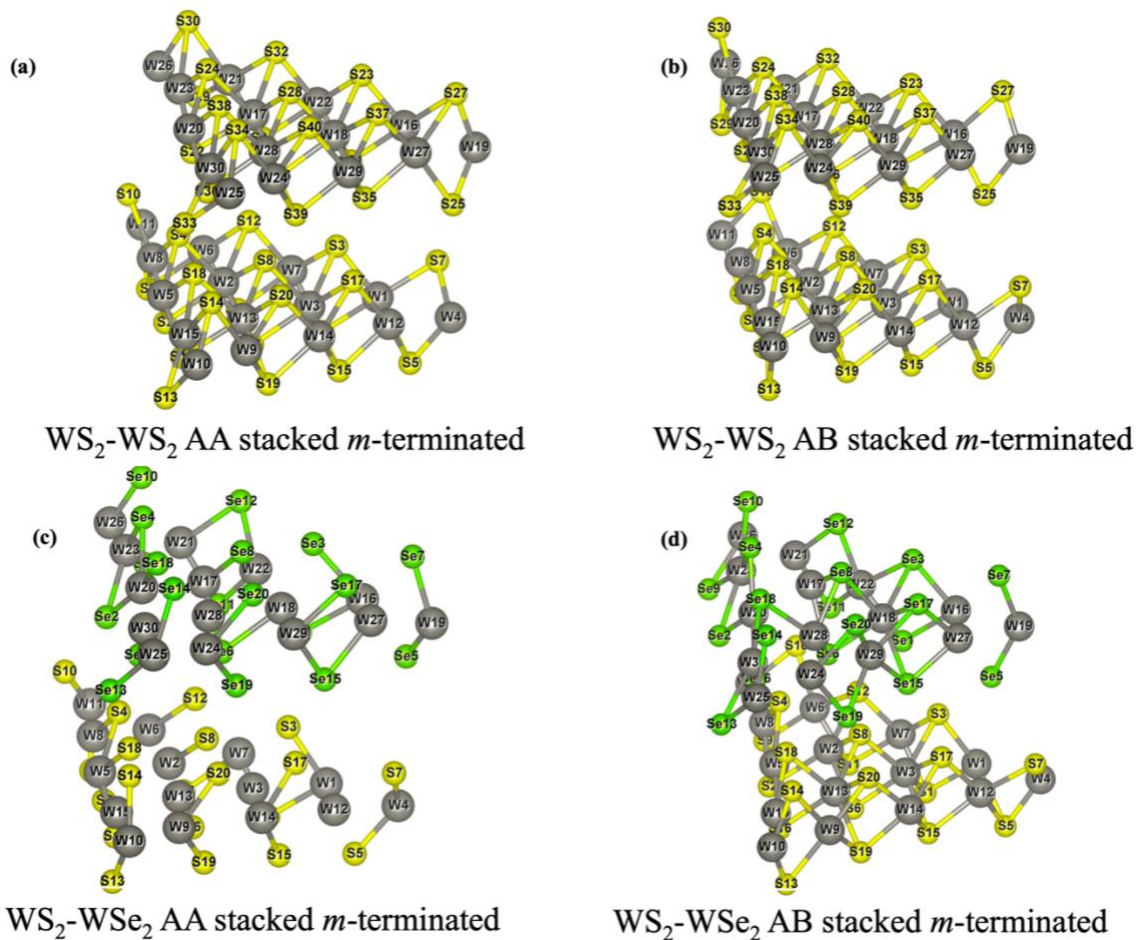


Fig. S3. Optimized labelled side views of a) *m*- terminated AA stacked WS_2 - WS_2 , b) *m*- terminated AB stacked WS_2 - WS_2 , c) *m*- terminated AA stacked WS_2 - WSe_2 and, d) *m*- terminated AB stacked WS_2 - WSe_2 .

Section S3. Bader Charge Analysis for the corresponding systems:

All the charges were tabulated based on the atoms number provided on Fig S2 and S3. The highest and lowest positively charged atom's electron partition were given in Red color and the negatively charged highest and lowest atom's electron partition were provided in Green color. Their corresponding charges were provided inside the bracket and in Blue color.

WS2-WS2 AA stacked c-terminated

<i>Atom number</i>	<i>Bader charge</i>
W_1	3.7922
W_2	3.7589
W_3	3.9923
W_4	3.4615
W_5	3.5019
W_6	3.758
W_7	3.5093
W_8	3.8072
W_9	3.7804
W_10	3.7658
W_11	3.7746
W_12	3.8198
W_13	4.0273 (+1.9727 e)
W_14	3.4712
W_15	3.5118
W_16	3.804
W_17	3.2494 (+2.7506 e)
W_18	3.7994
W_19	3.7856
W_20	3.7683
S_1	6.9879
S_2	6.8927

S_3	7.0206
S_4	6.8634
S_5	6.8692
S_6	6.3651
S_7	6.9586
S_8	6.7752
S_9	6.3498
S_10	7.0261
S_11	6.8733
S_12	6.8514
S_13	6.8569
S_14	6.839
S_15	6.7738
S_16	6.728
S_17	6.8421
S_18	6.8119
S_19	6.2582 (-0.2582 e)
S_20	6.2695
S_21	6.4046
S_22	6.4253
S_23	6.9701
S_24	6.8541
S_25	7.0187
S_26	6.7725

S_27	6.8647
S_28	6.8109
S_29	6.7748
S_30	6.7844
S_31	7.0063
S_32	6.8741
S_33	6.9732
S_34	6.8698
S_35	6.7764
S_36	6.3423
S_37	7.0006
S_38	6.8332
S_39	6.3697
S_40	6.9707
S_41	6.8096
S_42	6.8324
S_43	6.7561
S_44	6.7076
S_45	6.8631
S_46	6.8219
S_47	6.829
S_48	7.1884 (-1.884 e)
S_49	6.2587
S_50	6.3462

S_51	6.399
S_52	6.3202
S_53	7.012
S_54	6.7907
S_55	6.9717
S_56	6.8171
S_57	6.7525
S_58	6.778
S_59	6.8661
S_60	6.8319

WS2-WS2 AB stacked c-terminated

Atom number	Bader electron Charge partition
W_1	3.776
W_2	3.7835
W_3	4.028 (+1.972 e)
W_4	3.1061 (+2.8939 e)
W_5	3.3837
W_6	3.7844
W_7	3.1572
W_8	3.861
W_9	3.7764
W_10	3.7824
W_11	3.7439

W_12	3.8124
W_13	4.011
W_14	3.1863
W_15	3.271
W_16	3.7953
W_17	3.2411
W_18	3.8144
W_19	3.8133
W_20	3.7385
S_1	6.9723
S_2	7.1269 (-1.1269 e)
S_3	6.9892
S_4	6.7431
S_5	6.7817
S_6	6.2849
S_7	6.9731
S_8	6.7843
S_9	6.3191
S_10	6.99
S_11	6.7422
S_12	6.8866
S_13	6.8061
S_14	6.851
S_15	6.9563

S_16	6.8279
S_17	7.0715
S_18	6.7637
S_19	6.262 (-0.262 e)
S_20	6.429
S_21	6.4072
S_22	6.2779
S_23	6.9811
S_24	7.1218
S_25	6.98
S_26	6.7545
S_27	7.0399
S_28	6.826
S_29	6.7648
S_30	6.8089
S_31	7.0074
S_32	6.7348
S_33	6.9775
S_34	7.0797
S_35	6.751
S_36	6.3303
S_37	7.0178
S_38	6.7889
S_39	6.3761

S_40	6.9771
S_41	7.1069
S_42	6.7671
S_43	6.8052
S_44	6.8094
S_45	6.8459
S_46	6.8256
S_47	6.9622
S_48	6.7488
S_49	6.3112
S_50	6.4066
S_51	6.3402
S_52	6.392
S_53	6.9823
S_54	6.7491
S_55	6.9809
S_56	6.972
S_57	7.1025
S_58	6.8249
S_59	6.7743
S_60	6.8637

WS2-WSe2 AA stacked c-terminated

Atom_number	Bader electron Charge partition
-------------	------------------------------------

W_1	3.797
W_2	3.7474
W_3	3.9959
W_4	3.5276 (+2.4724 e)
W_5	3.3683
W_6	3.8111
W_7	3.5447
W_8	3.7824
W_9	3.7726
W_10	3.7833
W_11	4.3316
W_12	4.3383
W_13	4.5441 (+1.4559)
W_14	3.9669
W_15	4.1049
W_16	4.3398
W_17	4.0082
W_18	4.3071
W_19	4.3402
W_20	4.3256
S_1	6.9896
S_2	6.9105
S_3	7.0642
S_4	6.874

S_5	6.9015
S_6	6.3639
S_7	6.977
S_8	6.8133
S_9	6.364
S_10	7.0421
S_11	6.9375
S_12	6.8194
S_13	6.9777
S_14	6.8338
S_15	6.8115
S_16	6.7619
S_17	6.851
S_18	6.8159
S_19	6.4178
S_20	6.4134
S_21	6.2778
S_22	6.3209
S_23	6.9926
S_24	6.8791
S_25	7.0672 (-1.0672 e)
S_26	6.8285
S_27	6.8574
S_28	6.8456

S_29	6.871
S_30	6.7766
Se_1	6.7351
Se_2	6.669
Se_3	6.7035
Se_4	6.5131
Se_5	6.5011
Se_6	6.3058
Se_7	6.7287
Se_8	6.594
Se_9	6.284
Se_10	6.719
Se_11	6.5896
Se_12	6.5702
Se_13	6.622
Se_14	6.525
Se_15	6.5722
Se_16	6.6337
Se_17	6.524
Se_18	6.6461
Se_19	6.3137
Se_20	6.2616
Se_21	6.3028
Se_22	6.2462 (-0.2462 e)

Se_23	6.7441
Se_24	6.6438
Se_25	6.7278
Se_26	6.5215
Se_27	6.6308
Se_28	6.534
Se_29	6.5993
Se_30	6.6446

WS2-WSe2 AB stacked c-terminated

Atom_number	Bader electron Charge partition
W_1	3.8172
W_2	3.8055
W_3	4.0469
W_4	3.0693
W_5	3.0431 (+2.9569 e)
W_6	3.7794
W_7	3.5063
W_8	3.7834
W_9	3.7883
W_10	3.7839
W_11	4.3183
W_12	4.3459
W_13	4.5561(+1.4439 e)

W_14	4.0523
W_15	4.074
W_16	4.3104
W_17	4.0825
W_18	4.3383
W_19	4.3219
W_20	4.2984
S_1	6.9737
S_2	7.1226
S_3	7.0423
S_4	6.7926
S_5	6.83
S_6	6.333
S_7	6.9874
S_8	6.8127
S_9	6.3199
S_10	7.0374
S_11	7.0652
S_12	6.7993
S_13	7.1308
S_14	6.8391
S_15	6.813
S_16	6.7888
S_17	6.8474

S_18	6.8381
S_19	6.3101
S_20	6.3536
S_21	6.4066
S_22	6.42
S_23	6.9631
S_24	7.1364 (-1.1364 e)
S_25	7.0396
S_26	6.796
S_27	6.849
S_28	6.8576
S_29	6.9085
S_30	6.8442
Se_1	6.7079
Se_2	6.4865
Se_3	6.7408
Se_4	6.6889
Se_5	6.554
Se_6	6.2752
Se_7	6.7092
Se_8	6.6152
Se_9	6.2383
Se_10	6.7337
Se_11	6.6231

Se_12	6.5508
Se_13	6.6329
Se_14	6.5276
Se_15	6.5986
Se_16	6.6331
Se_17	6.5621
Se_18	6.56
Se_19	6.2596
Se_20	6.2189 (-0.2189 e)
Se_21	6.2993
Se_22	6.321
Se_23	6.7176
Se_24	6.5026
Se_25	6.7311
Se_26	6.6858
Se_27	6.6488
Se_28	6.542
Se_29	6.6215
Se_30	6.6344

WS₂-WS₂ AA stacked *m*-terminated

<i>Atom_number</i>	<i>Bader Charge</i>
W_1	4.5663
W_2	4.2158

W_3	4.2431
W_4	4.7545
W_5	4.3288
W_6	4.6824
W_7	4.4091
W_8	4.628
W_9	4.5508
W_10	4.8743
W_11	4.8599
W_12	4.6719
W_13	4.14
W_14	4.4481
W_15	4.6043
W_16	3.3687 (+2.6313 e)
W_17	4.2024
W_18	4.1992
W_19	4.8176
W_20	4.3493
W_21	4.5339
W_22	4.4124
W_23	4.7856
W_24	4.6933
W_25	4.9682
W_26	4.8853

W_27	5.8745 (+0.1255 e)
W_28	4.1641
W_29	4.303
W_30	4.622
S_1	7.0966
S_2	7.1012
S_3	7.1106
S_4	7.1054
S_5	7.1241
S_6	6.9867 (-0.9867 e)
S_7	7.2023 (-1.2023 e)
S_8	7.0216
S_9	7.1046
S_10	7.1554
S_11	7.0629
S_12	7.1326
S_13	7.1085
S_14	7.0579
S_15	7.0783
S_16	7.0714
S_17	7.0967
S_18	7.1049
S_19	7.1292
S_20	7.1387

S_21	7.1225
S_22	7.1246
S_23	7.0965
S_24	7.0561
S_25	7.1245
S_26	7.009
S_27	7.0983
S_28	7.011
S_29	7.1537
S_30	7.0837
S_31	7.1102
S_32	7.0801
S_33	7.1494
S_34	7.0445
S_35	7.1335
S_36	7.0984
S_37	7.0793
S_38	7.0923
S_39	7.1077
S_40	7.0784

WS2-WS2 AB stacked m-terminated

Atom_number	Bader Charge
W_1	4.4886
W_2	4.2469

W_3	4.2146
W_4	4.8674
W_5	4.4671
W_6	4.6867
W_7	4.2574
W_8	4.5256
W_9	4.4837
W_10	4.869
W_11	4.9025
W_12	4.7257
W_13	4.2139
W_14	4.3839
W_15	4.6559
W_16	5.8867 (+0.1133 e)
W_17	4.1813
W_18	4.1681
W_19	4.8505
W_20	4.3921
W_21	4.5962
W_22	4.3804
W_23	4.6607
W_24	4.7543
W_25	4.896
W_26	4.8297

W_27	3.3663 (+2.6337 e)
W_28	4.1753
W_29	4.4569
W_30	4.5708
S_1	7.1052
S_2	7.1353
S_3	7.1525
S_4	7.1465 (-1.1465 e)
S_5	7.083
S_6	6.9985
S_7	7.1324
S_8	7.019
S_9	7.0602
S_10	7.0799
S_11	7.0661
S_12	7.1753
S_13	7.0803
S_14	7.0791
S_15	7.0987
S_16	7.112
S_17	7.0955
S_18	7.1075
S_19	7.1464
S_20	7.138

S_21	7.0561
S_22	7.0859
S_23	7.1043
S_24	7.0741
S_25	7.0517
S_26	6.9975 (-0.9975 e)
S_27	7.1033
S_28	7.0087
S_29	7.1075
S_30	7.1329
S_31	7.1196
S_32	7.1283
S_33	7.1278
S_34	7.072
S_35	7.1308
S_36	7.0992
S_37	7.1386
S_38	7.1046
S_39	7.1049
S_40	7.0866

WS2-WSe2 AA stacked m-terminated

Atom_number	Bader Charge
W_1	4.6471
W_2	4.2029 (+1.7971 e)

W_3	4.2598
W_4	4.8404
W_5	4.308
W_6	4.6683
W_7	4.4788
W_8	4.6546
W_9	4.3201
W_10	4.9066
W_11	4.7937
W_12	4.5668
W_13	4.1933
W_14	4.329
W_15	4.773
W_16	4.9187
W_17	4.8499
W_18	4.762
W_19	5.1762 (+0.8238 e)
W_20	4.8153
W_21	4.7564
W_22	4.7219
W_23	4.9417
W_24	4.871
W_25	5.1712
W_26	5.1122

W_27	4.8267
W_28	4.6797
W_29	4.7626
W_30	4.8875
S_1	7.1153
S_2	7.0836
S_3	7.1358
S_4	7.091
S_5	7.0858
S_6	7.0045
S_7	7.1355
S_8	7.0303
S_9	7.0921
S_10	7.1645
S_11	7.0719
S_12	7.1066
S_13	7.0974
S_14	7.0696
S_15	7.1399
S_16	7.0856
S_17	7.1278
S_18	7.0921
S_19	7.1499
S_20	7.1658 (-1.1658 e)

Se_1	6.8588
Se_2	6.8967
Se_3	6.8725
Se_4	6.8416
Se_5	6.8907
Se_6	6.7453
Se_7	6.7924
Se_8	6.756
Se_9	6.8906
Se_10	6.7651
Se_11	6.814 (-0.814 e)
Se_12	6.8606
Se_13	6.8941
Se_14	6.8145
Se_15	6.8262
Se_16	6.8417
Se_17	6.8302
Se_18	6.8661
Se_19	6.8744
Se_20	6.8278

WS2-WSe2 AB stacked m-terminated

Atom_number	Bader Charge
W_1	4.7064
W_2	4.2549

W_3	4.1701
W_4	4.8452
W_5	4.5263
W_6	4.6113
W_7	4.3729
W_8	4.7298
W_9	5.9104 (+0.0896 e)
W_10	4.848
W_11	4.7699
W_12	4.6159
W_13	4.2307
W_14	4.3277
W_15	3.2404 (+2.7596 e)
W_16	4.8426
W_17	4.8483
W_18	4.6918
W_19	5.1919
W_20	4.5752
W_21	4.9508
W_22	4.81
W_23	4.9561
W_24	4.7622
W_25	5.1297
W_26	4.9477

W_27	4.7798
W_28	4.8141
W_29	4.8387
W_30	4.8014
S_1	7.0792
S_2	7.0448
S_3	7.1231
S_4	7.0686
S_5	7.0683
S_6	6.9849
S_7	7.1724 (-1.1724 e)
S_8	7.0104
S_9	7.1215
S_10	7.1466
S_11	7.0623
S_12	7.1017
S_13	7.0826
S_14	7.0867
S_15	7.0803
S_16	7.1168
S_17	7.1104
S_18	7.1305
S_19	7.0833
S_20	7.1158

Se_1	6.8252
Se_2	6.9682
Se_3	6.9057
Se_4	6.8218
Se_5	6.8117
Se_6	6.6598
Se_7	6.8225
Se_8	6.7499 (-0.7499 e)
Se_9	6.9719
Se_10	6.8909
Se_11	6.8703
Se_12	6.851
Se_13	6.9173
Se_14	6.8237
Se_15	6.8648
Se_16	6.872
Se_17	6.8819
Se_18	6.8758
Se_19	6.8956
Se_20	6.8299

